University of Kentucky
UKnowledge

Lewis Honors College Capstone Collection | Lewis Honors College

2020

Analysis of Magnetization Directions of Lunar Swirls

Lillie Cole
University of Kentucky, lilliecole@twc.com

Follow this and additional works at: https://uknowledge.uky.edu/honprog

 Part of the Other Physics Commons

Right click to open a feedback form in a new tab to let us know how this document benefits you.

Recommended Citation

Cole, Lillie, "Analysis of Magnetization Directions of Lunar Swirls" (2020). *Lewis Honors College Capstone Collection*. 46.
https://uknowledge.uky.edu/honprog/46

This Article is brought to you for free and open access by the Lewis Honors College at UKnowledge. It has been accepted for inclusion in Lewis Honors College Capstone Collection by an authorized administrator of UKnowledge. For more information, please contact UKnowledge@lsv.uky.edu.

Analysis of Magnetization Directions of Lunar Swirls

L. Cole

Honors Capstone Project Advisor: Prof. D. Ravat

University of Kentucky

Abstract: Lunar Swirls are high albedo markings on the Moon that exist in the regions of some crustal magnetic anomalies. The precise mechanism responsible for the swirl features is unknown but a prevailing theory is solar wind standoff, where the magnetic field from subsurface magnetized sources protects the lunar surface from solar wind ions, leading to their lesser maturation and brighter appearance. If this theory is correct, the magnetic field of the anomalies should heavily influence the appearance of the swirl. To better understand the cause of swirls, the magnetization direction of the source creating the field is analyzed. This study uses differences of the vector fields measured along satellite orbits (20-40 km above the lunar surface), which have lesser noise because time-varying external fields in the lunar environment are nearly the same for short times between consecutive data points. The magnetization of the magnetic features is derived by best-fitting fields from a set of unidirectional magnetized dipoles. The best-fit is judged by comparing computed vector fields with the observed vector fields (their misfit) and their correlation coefficient. Magnetization directions of the magnetic features analyzed in the study do show a strong relationship between the magnetization directions and the appearance of the swirl. After obtaining the magnetization directions, the corresponding magnetic paleopoles were determined. The paleopole locations do not coincide with the current rotational axis of the Moon (assuming a dipolar core field) and are fairly spread out over the Moon. If the Moon did possess an early dipolar core dynamo then it was most likely not aligned with the present rotational axis. The uncertainty in the magnetization directions and derived paleopole locations as judged by best-fit magnetization directions using different criteria is fairly large.

1. Introduction

Rocks become magnetized when their magnetic minerals align with the direction of an ambient field and can retain their magnetization direction acquired at the time of formation even after the external field is removed (Butler, 1992). The Moon does not currently have a core dynamo driven magnetic field, but many crustal magnetic anomalies have been observed (Figure 1). Some of these anomalies are associated with bright, high-albedo markings that do not correlate with the Moon's topography, geology, and gravity anomalies (Blewett et al., 2010; Hemingway and Tikoo, 2018). These features are referred to as lunar swirls and the appearance of the swirls can be complex. Some swirls have distinct bright areas and narrow dark lanes like the Reiner Gamma swirl, and others can be diffuse like the one seen associated with the Descartes magnetic anomaly (Blewett et al., 2011). Images of swirls and their magnetic anomalies investigated in this study are presented in later figures.

The mechanism that causes lunar swirls is not well-understood but there are three main proposed formation theories. One model suggests that the swirls are caused by solar wind standoff. In this mechanism, the bright patterns of swirls are caused by reduced space weathering from solar wind ions which, if unimpeded, would affect the optical properties and darken the exposed surfaces as it does normally on the Moon. If the magnetic field lines are open or perpendicular to the Moon's surface then this would allow for normal space weathering on the surface, but closed or horizontal field lines (perpendicular to the solar wind) will deflect the solar wind ions and allow the Moon's surface to retain its normal brightness (Hemingway and Tikoo, 2018). Another proposed mechanism of swirl formation

is from cometary impacts where the swirl features are caused by scouring of the Moon's surface (Blewett et al., 2011; Glotch et al., 2015). The third major mechanism invokes dust transportation and postulates that the high-albedo areas are caused by the levitation and transportation of fine-grained particles in the presence of an electric or magnetic field (Hemingway and Tikoo, 2018; Glotch et al., 2015). Near-infrared observations of the lunar swirls show that they are less optically mature than the surrounding areas which supports the solar wind standoff theory (Glotch et al., 2015).

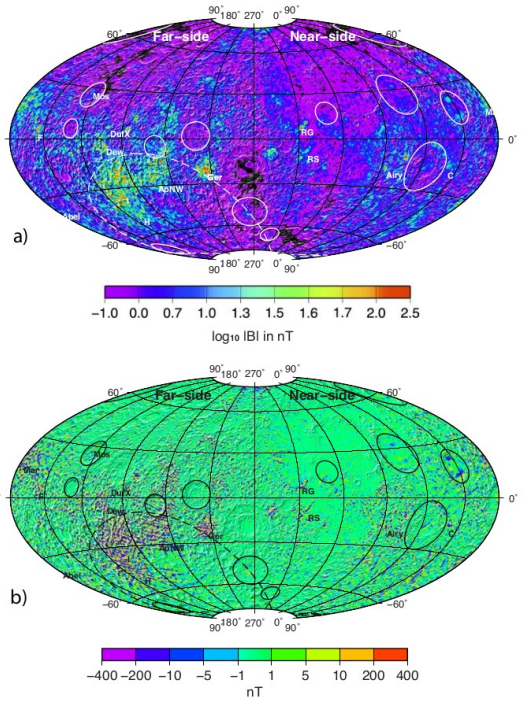

FIG. 1: The surface magnetic fields from the global magnetic field model of Ravat et al. (2020). a) the total field and b) the radial component of the magnetic field. Ovals represent Nectarian basins, dashed oval is the South Pole-Aitken basin. Some swirl features studied here are also labeled. RG-Reiner Gamma, Ger-Gerasimovich, RS – Rima Sirsalis.

If the swirl patterns are caused by the deflection of solar wind ions, then their appearance should be heavily dependent on the magnetic field near the Moon's surface (Hemingway and Tikoo, 2018). A better understanding of the source magnetization can help to determine if this formation theory is correct. Studying the magnetic anomalies associated with swirls can also give insight into the magnetic history of the Moon. Lunar Prospector (LP) data shows that there are strong magnetic anomalies (w.r.t. the background regions) distributed across the lunar surface (Oliveira and Wieczorek, 2017) and it is believed that the Moon had a planetary magnetic field existing 3.5-4 Ga with intensities up to 10-100 μT (Arkani-Hamed and Boutin, 2014; Weiss and Tikoo, 2014). While the idea of a core dynamo field is widely accepted, the origin of the field that magnetized the surface is still debated. It has also been proposed that the crustal fields could have been created or amplified during impact events and this is supported by the fact that some of the magnetic anomalies are antipodal to impact basins (Hood and Huang, 1991; Hood and Artemieva, 2008). In general, three magnetizing mechanisms have been considered: impact-related magnetization, magnetization by early solar wind field, and magnetization by an early core dynamo (Arkani-Hamed and Boutin, 2014; Oliveira and Wieczorek, 2017). Once the magnetization direction of each anomaly has been found, the corresponding paleopole location of the selenocentric dipole can be determined. If the paleopole locations are clustered or if they show trends consistent with reversing fields, then that would be strong evidence for a dynamo generated field (Oliveira and Wieczorek, 2017).

Previous studies have considered isolated magnetic anomalies using either field maps (Oliviera and Wiezorick, 2017) or actual data distributions of magnetic vector data (Arkani-Hamed and Boutin, 2014), while in this study we used along-orbit differences of the vector data (also called gradients here). The gradient fields were created from the vector data by taking the difference of two near-by locations and were used to suppress the effects of external fields and possibly other long-wavelength artifacts in the vector data (Ravat et al., 2020). Similar to the magnetic study of Oliveira and Wieczorek (2017), no assumptions were made about the source geometry and the only assumption made is that unidirectional equivalent source dipoles form the anomaly. The magnetization direction of the dipoles and their depth is also varied to recover the best-fitting model (in contrast, Oliveira and Wieczorek, 2017, used dipoles at the surface).

The manuscript is organized as follows: Section 2 describes the method used to model the chosen magnetic anomalies and the procedures for selecting the best-fitting models. Section 3 discusses the modeling results and the associated paleopole location for each anomaly. Section 4 discusses the results and possibilities for future work.

2. Method

In this study, six magnetic anomalies were examined/modeled; they are Reiner Gamma, Serenitatis, Descartes, Airy, Gerasimovich, and Rima Sirsalis. For each feature, it was assumed that the magnetic anomaly was created by dipoles having spatially varying magnetization strengths but all magnetized in the same direction. The best-fitting inclination and declination were found through the inversion of magnetic anomalies and the radial component was used when considering the best-fitting field. The radial field was used because it represents nearly all of the key information about the field measured in a source free region well (Ravat et al., 2020).

First, equal area dipoles were spread evenly in the region being analyzed with a dipole spacing of 0.4°. Oliveira and Wieczorek (2017) showed that the modeled field had noticeable edge effects when the radii of dipoles (r_s) and observations (r_a) were the same; these effects did not appear when the circles of observations were 1° or 1.5° larger in radius than the circle of dipoles. For this study, we verified the edge effect and used a 1° difference in the radii.

The main reason for using the gradient field in this study was to reduce the effects of external noise in the observations. External fields that appear in the vector data are nearly the same for consecutive data points (which are five seconds apart in the data we used), so their effect on derived parameters (i.e., magnetic moments, inclination, and declination) is minimized when the along-orbit differences are used. The decrease in noise can be seen in Figure 2 where the vector and gradient data are compared for the magnetic anomaly of Reiner Gamma. The features of the field are easier to distinguish in the gradient field than the vector field.

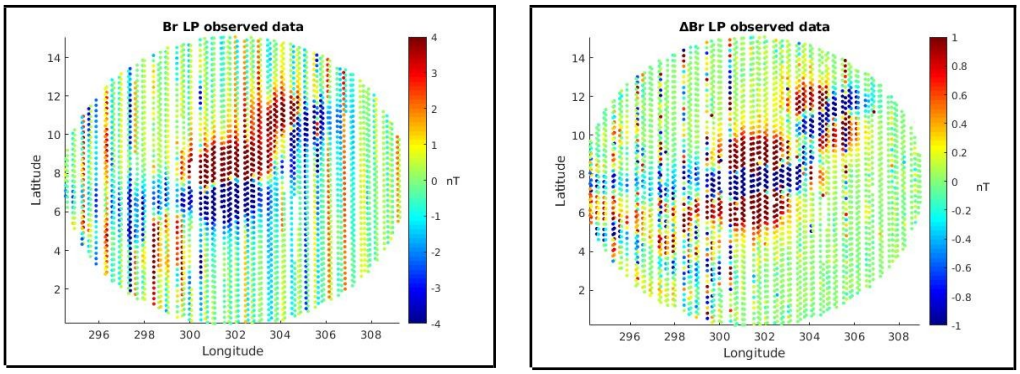

FIG. 2: The observed Lunar Prospector (LP) vector radial field (left) and radial along-track gradient field (right) for the Reiner Gamma swirl. On the vector data, there are large differences from one orbit to the next and those differences are artifacts from varying amounts of external fields in different orbits or other long-wavelength effects. Such differences do not occur in the gradient field and the only artifacts that are present are short wavelength speckled noise. The decrease in noise can also be seen from the color bar scale differences between the vector and gradient plots.

All model studies and real data inversions used for recovering inclinations and declinations of magnetization in this study used along-orbit differences of the fields. Appendices A.1 and A.2 show the model studies of this recovery using four different methods involving comparisons of observed and computed Br and ΔBr and also calculated vector and gradient fields using directionally unconstrained

dipoles used as “observed” fields. (Directionally unconstrained dipoles fit the fields better as combinations of differently oriented dipoles have lesser constraints in fitting the field.) The latter was done to primarily avoid the effects of noise in the best-fit RMS and correlation coefficient criteria used for determining the inclination and declination of magnetization. Of the four kinds of data being fit, three consistently performed well in the recovery of inclination and declination of magnetization (calculated vector fields did not perform well). Of the three that performed well, one of them involved simulated observed and computed Br fields but since the actual observed Br data are nearly always noisy, this approach was not used. The remaining two methods are named Methods 1 and 2 and are discussed in more detail below.

Method 1 used the calculated gradient field as the input field with altitudes of 60 km or less. The calculated field was created by placing 0.6° equal area spacing equivalent source dipoles over the region and their magnetization direction was allowed to vary between each dipole. Method 2 used Lunar Prospector observation/ based along-track gradient data with an altitude of 60 km or less. In the determination of the best magnetization direction for the source, all magnetic inclination and declination values at an interval of 5° were examined where the inclination ranged from -90° to 90° and the declination ranged from -180° to 180°. The inclination and declination values were further narrowed down by examining around the best-fitting directions at an interval of 1°. The best-fitting directions were determined by minimizing the root mean square (RMS) of the observed and computed ΔBr component of the field while simultaneously attempting to maximize their correlation coefficient (R). Different depths of equivalent dipoles were also considered, starting at the surface and increasing the depth by 5 km, until the depth where the minimum RMS value was reached. The correlation coefficient determines the phase difference between the two quantities which are observed and the modeled field in this study. An R value of 1 corresponds to a phase difference of zero while values of 0 and -1 correspond to phase differences of 90° and 180°, respectively.

Once the best-fitting magnetization direction was obtained for each method the paleopole location was determined. In this study, the north paleopole or the negative planetocentric dipole location was calculated. The equations used to calculate the paleopole location are given in Appendix B.

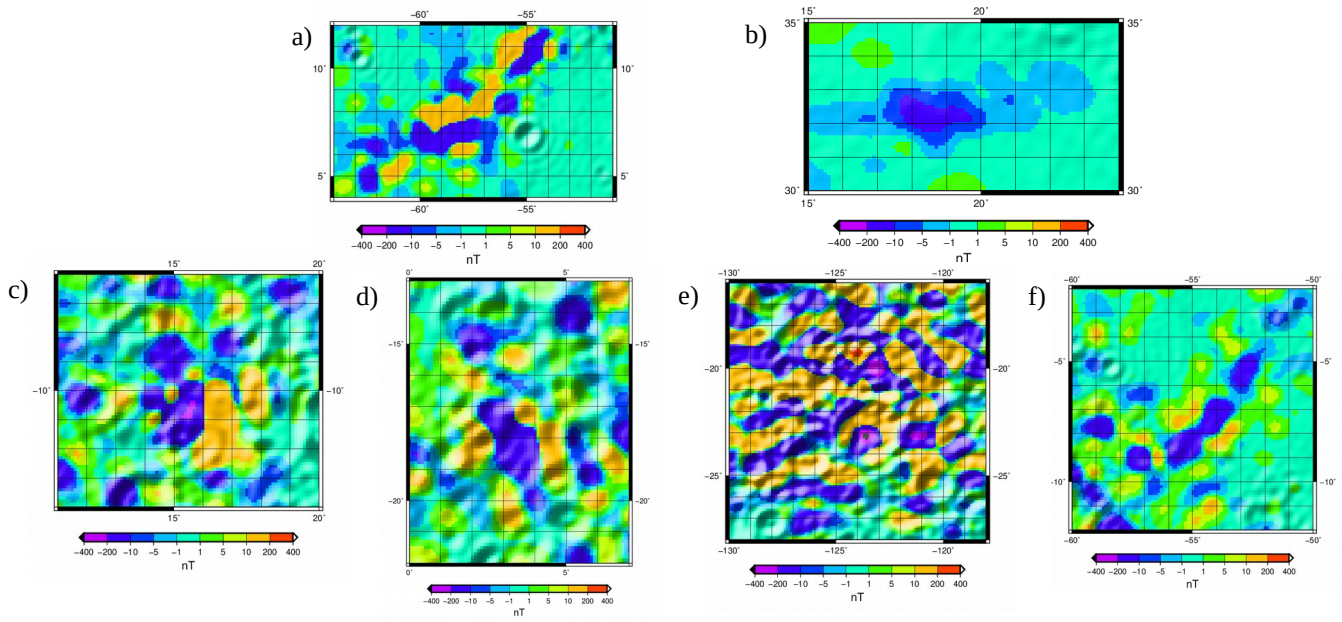

FIG. 3: The radial components of the magnetic anomalies modeled at the Moon’s surface (Ravat et al., 2020).
a) Reiner Gamma; b) Serenitatis; c) Descartes; d) Airy; e) Gerasimovich; and f) Rima Sirsalis.

3. Analysis and Results

3.1 Reiner Gamma

The Reiner Gamma swirl consists of two main magnetic anomalies. There is a larger, central anomaly and a smaller, northeastward trending anomaly to the northeast of the main anomaly in the center of Figure 3a. From the magnetic vector data for Reiner Gamma, it can be seen that the northeastern anomaly could be modeled with a more negative declination than the larger, central anomaly (the declination value can be estimated by connecting the negative lobe in the Br field to the positive lobe and estimating the angle that this line makes with North). Since we wanted to model the entire anomaly with a single magnetization direction, we first found the best-fitting direction from modeling the larger anomaly and modeled the entire anomaly with that declination value.

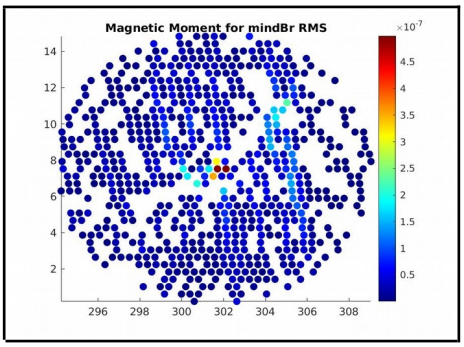

FIG. 4: The magnetic moments of the dipoles in Am^2 for Reiner Gamma. Red indicates more strongly magnetized dipoles.

Figure 4 shows that the northeastern anomaly can be modeled well by a lower declination if it is modeled as elongated, northeastward trending sources. Both methods of determining the best-fitting inclination and declination of magnetization gave an inclination value close to zero and a slightly negative declination value. The results of Table 1 show that Reiner Gamma is best modeled with a near horizontal field. The calculated paleopole locations for both methods give similar results.

TABLE 1: The best fitting magnetization directions for each method of determining magnetization direction along with the associated paleopole location. The location of the site used to determine the paleopole location was chosen visually at the center of the observed radial data (7.6° N and 302° E). This location is also close to the location of the strongest dipoles in Figure 4. The central anomaly was modeled with r_s of 4° and r_a of 5° while the entire Reiner Gamma anomaly was modeled with r_s of 7.5° and r_a of 8.5°. r_s and r_a are the radii of dipole sources and observations, respectively, considered in the inversion.

Method	Depth (km)	Incl (°)	Decl (°)	ΔBr RMS	R	Paleopole Location	Max R	Max R Incl (°)	Max R Decl (°)	Max R Paleopole Location
1	5	7	-12	0.567	0.9796	77.4°N 193.8°E	0.9796	7	-12	77.4°N 193.8°E
2	0	-16	-10	1.037	0.9478	71.4°N 154.5°E	0.9478	-16	-10	71.4°N 154.5°E

3.2 Serenitatis

Serenitatis is not a magnetic anomaly that has an associated lunar swirl, but it was examined because its magnetic field seems to imply that it should have a near vertical magnetization direction. The single negative lobe for the radial magnetic field (Figure 3b) would mean that the magnetization should have high inclination and hence the paleopole location would be close to the site location. Serenitatis anomaly is presently located near 32.5°N, 18.5°E, a location away from the current rotational axis. If it is modeled with a near vertical magnetization direction this could support the Moon having a core dynamo field that did not align with the present rotational axis or that the anomaly became magnetized when the field was reversing. Both Method 1 and Method 2 yielded an inclination value for Serenitatis that was 8°-10° higher than the results derived from the study of Oliveira and Wieczorek (2017). The results of this study are shown in Tables 2a and 2b.

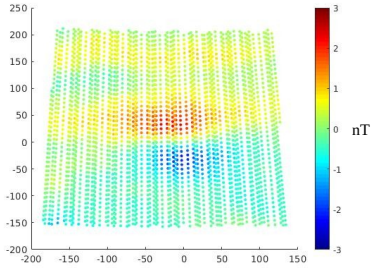

FIG. 5: The theta component of the calculated field for Serenitatis.

Since Serenitatis anomaly (Figure 5) can be modeled with a higher inclination than Oliveira and Wieczorek (2017), the declination value is not well constrained and multiple declination values could model the field well. Hence we use another method to fix the declination. The theta component on the vector magnetic field (Figure 5), in this case, can be used to gain insight into the declination value (i. e., the angle between the line connecting the centers of the negative and positive lobes and North, should be close to the magnetization declination). The angle is 24° west of North. Interestingly, this value is close to the declination derived by Oliveira and Wieczorek (2017). By keeping the declination value fixed the inclination value increased for Method 2 (i.e., using observed along-track gradients in the inversion) but decreased for Method 1 (i.e., using the modeled along-track gradients in the inversion). The values for the best-fitting direction when the declination was not kept fixed are shown in Table 2a. The results for the fixed declination case are shown in Table 2b. When the declination was fixed, the value from Method 1 gave a result similar to Oliveira and Wieczorek (2017), whereas Method 2 with fixed declination leads to a paleopole that is in the nearside mare region (in the Procellarum KREEP Terrain).

TABLE 2a: The magnetization direction and paleopole location for Serenitatis for both methods. The site location of 32.2° N and 18.5° E was used to calculate the paleopole location. Serenitatis was modeled with r_s of 3.5° and r_a of 4.5°.

Method	Depth (km)	Incl (°)	Decl (°)	ΔBr RMS	R	Paleopole Location	Max R	Max R Incl (°)	Max R Decl (°)	Max R Paleopole Location
1	5	76	63	0.039	0.9862	40.4°N 49.98°E	0.9864	71	89	26.6°N 57.8°E
2	25	74	-58	0.199	0.7192	43.3°N 343.1°E	0.7192	74	-58	43.3°N 343.1°E

TABLE 2b: The magnetization direction and paleopole location for Serenitatis for both methods with fixed declination.

Method	Depth (km)	Incl (°)	Decl (°)	ΔBr RMS	R	Paleopole Location	Max R	Max R Incl (°)	Max R Decl (°)	Max R Paleopole Location
1	5	69	-24	0.043	0.979	63.3°N 345°E	0.9791	67	-24	65.0°N 339.9°E
2	25	79	-24	0.199	0.7199	51°N 5.0°E	0.722	38	-24	66.1°N 267.5°E

3.3 Descartes

For Descartes, the radial component vector data at the surface from Figure 3c seems to imply that Descartes should be modeled with a low inclination and a declination that is greater than 90°. Table 3 shows that the recovered direction for Descartes is a low inclination with a declination of 100°. The results from the two methods are very close to each other and give almost identical paleopole locations.

TABLE 3: The magnetization direction and paleopole location for Descartes for both methods. The site location of 10.5° S and 16° E was used to calculate the paleopole location. An equivalent source radius r_s of 4° and observation radius r_a of 5° were used.

Method	Depth (km)	Incl (°)	Decl (°)	ΔBr RMS	R	Paleopole Location	Max R	Max R Incl (°)	Max R Decl (°)	Max R Paleopole Location
1	0	16	100	0.277	0.9816	11.2°S, 99.7°E	0.9816	16	100	11.2°S 99.7°E
2	0	17	100	0.401	0.9620	11.3°S, 99.1°E	0.9620	17	99	10.3°S 99.0°E

3.4 Airy

For the previous anomalies, the equivalent source location was chosen to only include the magnetic anomaly that was associated with the lunar swirl feature. The Airy magnetic anomaly is not as well isolated as the previous anomalies, so a slightly larger area was used to make sure that the entire feature was included. Figure 3d shows the magnetic anomaly at the surface for Airy and that there is a strong negative lobe, but also some other magnetic features nearby that could have been magnetized at the same time. The magnetic anomaly at Airy is similar to Serenitatis since it also contains a strong negative lobe, but in this case, there appear to be multiple anomaly features in the region and it would be difficult to judge the magnetization direction.

Table 4 shows that Airy is modeled well with a higher inclination but the results from Method 1 and 2 give different paleopole locations. The paleopole locations for Method 2 indicate that the pole location was very close to the swirl location. The fact that the results of both methods yield a high correlation coefficient value shows that the range of possible inclinations for Airy is large. The cause of the disparate results is likely to be the complexity of sources in the region. Further investigation of this source would be useful.

TABLE 4: The magnetization direction and paleopole location for Airy for both methods. The site location of 17° S and 2.2° E was used to calculate the paleopole location. For Airy, r_s was 5° and r_a was 6°.

Method	Depth (km)	Incl (°)	Decl (°)	ΔBr RMS	R	Paleopole Location	Max R	Max R Incl (°)	Max R Decl (°)	Max R Paleopole Location
1	0	62	141	0.206	0.9608	47.9°S 45.3°E	0.9608	62	141	47.9°S 45.3°E
2	5	85	104	0.389	0.8101	19.1°S 12.4°E	0.8791	85	129	23.1°S 10.6°E

3.5 Gerasimovich

For Gerasimovich, an area was selected so that all anomaly features were included. Table 5 shows that Gerasimovich is modeled well with an inclination of around 45° and a low value declination.

TABLE 5: The magnetization direction and paleopole location for Gersasimovich for both methods. The site location of 22° S and 236.7° E was used to calculate the paleopole location. A radius r_s of 5° and r_a of 6° were used.

Method	Depth (km)	Incl (°)	Decl (°)	ΔBr RMS	R	Paleopole Location	Max R	Max R Incl (°)	Max R Decl (°)	Max R Paleopole Location
1	0	42	8	0.520	0.9642	43.1°N 246.7°E	0.9642	41	7	44.0°N 245.6°E
2	0	46	18	0.686	0.9395	37.6°N 257°E	0.9396	45	19	38.1°N 258.4°E

3.6 Rima Sirsalis

For Rima Sirsalis, Table 6 shows that the anomaly is modeled well with an inclination of around 40° and a declination near 145°. The results from Methods 1 and 2 give similar paleopole locations.

TABLE 6: The magnetization direction and paleopole location for Rima Sirsalis for both methods. The site location of 7.5° S and 305.3° E was used to calculate the paleopole location. A radius r_s of 4° and r_a of 5° were used.

Method	Depth (km)	Incl (°)	Decl (°)	ΔBr RMS	R	Paleopole Location	Max R	Max R Incl (°)	Max R Decl (°)	Max R Paleopole Location
1	0	44	150	0.224	0.9129	56.1°S 359.1°E	0.9129	42	149	55.9°S 2.3°E
2	0	37	146	0.326	0.8365	54.6°S 9.9°E	0.8365	36	146	54.8°S 11.0°E

3.7 Analysis of Paleopoles

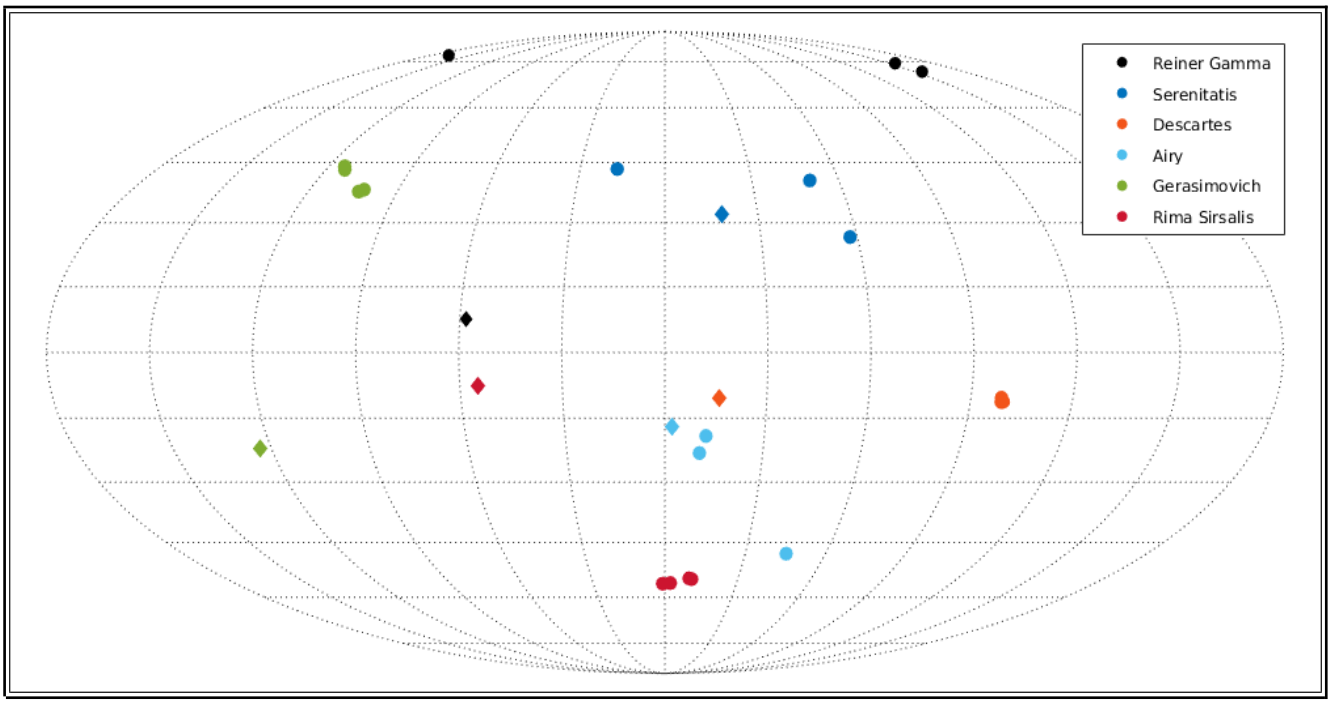

FIG. 6: The paleopole locations for each anomaly are represented by circles and the site locations are represented by diamonds. Molleweide projection centered on 0° E.

Figure 6 shows that the paleopole locations are not clustered around a single location or an antipodal location. The paleopole locations are fairly spread out across the Moon. For the majority of anomalies, the locations recovered from both methods are clustered around a similar area (even Reiner Gamma which only appears to be spread out as the map projection is centered on 0° longitude and the paleopoles are located near the pole). The two anomalies that do not give similar paleopole locations between the methods are Serenitatis and Airy. Both of these anomalies were modeled with a higher inclination and had a wider range in declination values. For these anomalies, their mean paleopole location was determined.

To calculate the mean paleopole location all magnetization directions that produced an RMS value that was within 0.01 nT of the minimum RMS were converted to a pole location and these locations were averaged. The results for Serenitatis and Airy are shown in Table 7a and the averages of the paleopoles computed from the two methods are more similar. The mean locations were also considered for the other anomalies, but the paleopole locations did not significantly change. When there is a wide range of

possible magnetization directions for an anomaly but their fit is similar, it could be more meaningful to instead use the mean paleopole location. A different result is found if the paleopole location is determined from the mean inclination and declination and these results are shown in Table 7b. Finding the paleopole from the mean magnetization direction increases the paleopole latitude for all anomalies.

TABLE 7a: The mean paleopole locations for Serenitatis and Airy. The standard deviations for each value are shown in parenthesis.

Anomaly	Method	Mean Paleopole Latitude (°)	Mean Paleopole Longitude (°)
Serenitatis	1	33.87 N (22.95)	20.01 E (52.07)
	2	28.61 N (27.82)	17.60 E (70.55)
Serenitatis (fixed declination)	1	60.90 N (10.45)	316.88 E (41.69)
	2	59.04 N (9.16)	292.52 E (48.34)
Airy	1	29.99 S (22.27)	356.56 E (35.49)
	2	19.85 S (23.58)	6.02 E (30.36)

TABLE 7b: The paleopole location found from the mean magnetization inclination and declination within the 0.01 nT range of the minimum radial RMS value.

Anomaly	Method	Paleopole Latitude (°)	Paleopole Longitude (°)
Serenitatis	1	71.69 N	31.78 E
	2	86.92 N	36.18 E
Serenitatis (fixed declination)	1	69.24 N	316.62 E
	2	67.79 N	275.72 E
Airy	1	15.26 N	6.55 E
	2	20.48 N	356.31 E

4. Discussion

From the five anomalies studied associated with lunar swirls (all but Serenitatis), it can be seen that the anomalies that are modeled with a horizontal magnetization direction (near parallel to Moon's surface and perpendicular to the solar wind) have a more distinct swirl pattern. Reiner Gamma and Descartes have the brightest swirl features and are both modeled well with a near horizontal inclination and this is what is expected if solar wind standoff is the main cause for the appearance of lunar swirls. Airy has a higher inclination and its associated swirl is not as bright which shows that more vertically magnetized features are not as good at protecting the surface from solar weathering. The swirls at Gerasimovich and Rima Sirsalis are not as well defined as the one at Reiner Gamma and are not as bright as the swirls for Reiner Gamma and Descartes, but they are more visible than the swirl associated with Airy. They are both modeled well with an intermediate inclination which would not provide as much protection from space weathering as a horizontal field but does provide more protection than a near vertical field. The reason that Serenitatis anomaly region does not have a swirl could be its near-vertical magnetization.

The paleopoles are not located around a single location or clustered around a location. The locations are spread out and there are a few that are located closer to the Moon's equator. The distribution of paleopole locations could indicate that if there was a core dynamo, it was not aligned with the present rotational axis or that there was a change in the rotational axis. It is also possible that an anomaly could

have been magnetized while the field was reversing (Oliveira and Wieczorek, 2017) or experienced a core field excursion.

Further research will include examining more magnetic anomalies associated with swirls to investigate if there continues to be a correlation between the magnetization direction and how well defined the swirl feature is. Other well-isolated magnetic anomalies should be studied to determine additional paleopole locations to examine if they support the feasibility of an early core dynamo and help elucidate its evolution. It would also be beneficial to look at the impact features around different anomalies and the time estimates for these impacts since they could demagnetize near-surface regions affected by heat and pressure from impacts. Such cases would affect the recovered magnetization.

More work also needs to be done to determine the errors in the magnetization directions from the RMS and R values. Since the correlation coefficient describes the phase difference between the input and modeled field, there may be a cutoff value that determines how much of a phase difference is too large and this needs further investigation.

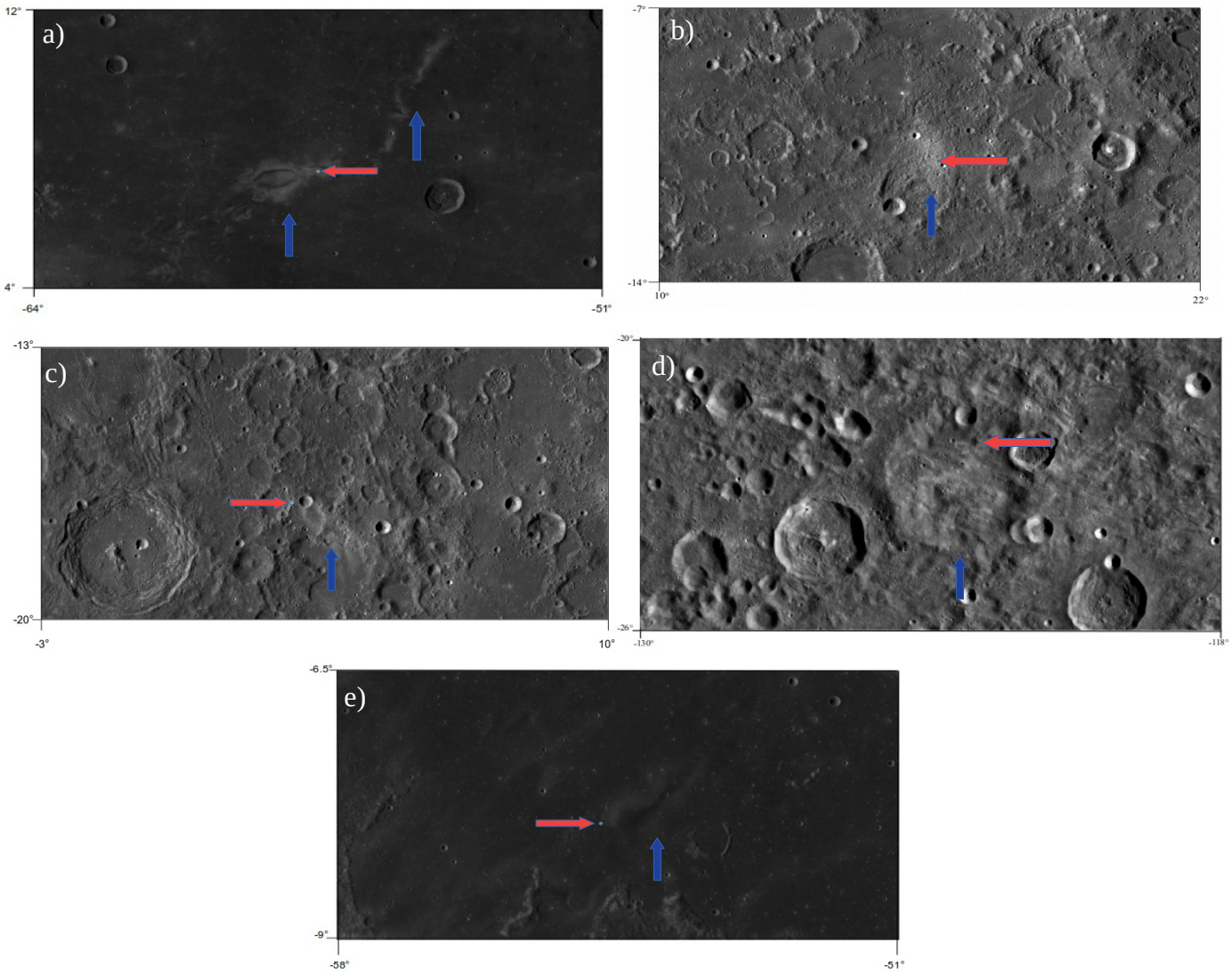

FIG. 7: Visual images of the swirls associated with the magnetic anomalies studied. a) Reiner Gamma; b) Descartes; c) Airy d) Gerasimovich; e) Rima Sirsalis. The red arrows point to the center of the magnetic anomalies while the blue arrows point to the swirl features.

Acknowledgments and Data

This study used data collected from the Lunar Prospector mission. I would like to thank Dr. Ravat for allowing me to use his lunar magnetic field models and for his review and feedback on this paper. This research was partly funded by NASA grant NNX16AN51G.

References

Arkani-Hamed, J., Boutin, D., 2014, Analysis of isolated magnetic anomalies and magnetic signatures of impact craters: Evidence for a core dynamo in the early history of the Moon. *Icarus,* 237, 262-277, doi:10.1016/j.icarus.2014.04.046.

Blewett, D. T., Denevi, B. W., Robinson, M. S., Ernst, C. M., Purucker, M. E, Solomon, S. C., 2010. The apparent lack of lunar-like swirls on Mercury: Implications for the formation of lunar swirls and for the agent of space weathering. *Icarus* 209, 239-246.

Blewett, D. T., Coman, E. I., Hawke, B. R., Gillis-Davis,J. J., Purucker, M. E., Hughes, C. G., 2011, Lunar swirls: Examining crustal magnetic anomalies and space weathering trends. J. Geophys. Res., 116, E02002, doi:10.1029/2010JE003656.

Butler, R. F., 1992. Origins of natural remanent magnetism. In Paleomagnetism: Magnetic Domains to Geological Terranes, (pp. 31-63). Oxford: Blackwell Scientific Publications

Garrick-Bethell, I., Head, J. W., Pieters, C. M., 2011. Spectral properties, magnetic fields, and dust transport at lunar swirls. *Icarus 212*, 480-492. doi:10.1016/j.icarus.2010.11.036

Glotch, T. D. et al., 2015. Formation of lunar swirls by magnetic field standoff of the solar wind. Nat. Commun. 6:6189 doi: 10.1038/ncomms7189.

Hemingway, D.J., Tikoo, S. M., 2018. Lunar swirl morphology constrains the geometry, magnetization, and origins of lunar magnetic anomalies. *Journal of Geophysical Research: Planets,* 123. http://doi.org/10.1029/2018JE005604

Hood, L.L., Huang, Z., 1991. Formation of magnetic anomalies antipodal to lunar impact basins: Two-dimensional model calculations. *Journal of Geophysical Research: Solid Earth,* 96. https://doi.org/10.1029/91JB00308

Hood, L.L., Artemieva, N.A., 2008. Antipodal effects of lunar basin-forming impacts: Initial 3D simulations and comparisons with observations. *Icarus* 193, 485-502. https://doi.org/10.1016/j.icarus.2007.08.023

Oliveira, J. S., Wieczorek, M. A., 2017, Testing the axial dipole hypothesis for the Moon by modeling the direction of crustal magnetization, *Journal of Geophysical Research: Planets*, 122, 383–399, doi:10.1002/2016JE005199.

Ravat, D., Purucker, M. E, Olsen, N., 2020. Lunar magnetic field models from Lunar Prospector and SELENE/Kaguya along-track magnetic field gradients. *Journal of Geophysical Research: Planets. 125, e2019JE006187. https://doi.org/ 10.1029/2019JE006187*

Appendices

A.1 Testing method using simulated fields

I tested the ability of the methods for correctly inverting magnetization directions using model simulations with known magnetization directions. Example fields were created by defining a simple rectangular prism. The depth of the source top and bottom and latitude and longitude coordinates were defined for the source. Once the model shape was defined, it was given a magnetization direction and the components of the magnetic field were calculated. Noise was then added to the data in the form of white Gaussian noise with a signal to noise ratio (SNR) of 10 and these were used as the 'observed fields'. Using the field with noise, a calculated field was produced using the same procedure described in section 2. The method described in section 2 was also used to find the best-fitting direction and this direction was determined by comparing the modeled field using equivalent source dipoles to the observed vector and gradient data along with the calculated vector and gradient data. The method of non-negative least squares was used in the inversion to determine the magnetization parameters. At each depth of dipoles placement, best-fitting magnetization was found based on the minimum radial field RMS and the maximum correlation coefficient R between the input and modeled field. Four different example fields were created to test the method. The magnetization directions and depths of the sources used to create the four different fields are shown in Table A.1. The first three have high magnetization inclinations, but varied declination. The fourth source has a low magnetization inclination. The radial component of the forward modeled fields is shown in Figure A.1.

TABLE A.1: The magnetization inclination, magnetization declination, and source depths used to create the four example fields. The source depth is measured positive below the surface.

Example Field	Inclination (°)	Declination (°)	Source top and bottom depths (km)
1	88	-25	0-10
2	72	45	10-15
3	83	133	25-30
4	-5	-25	3-7

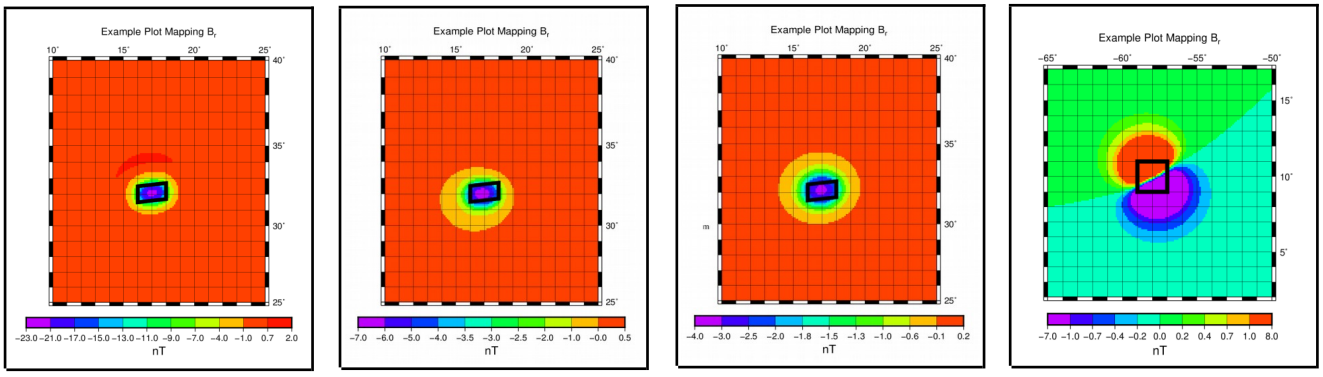

FIG. A.1: The radial magnetic component of the forward modeled fields before noise was added. The fields are shown in order with example field 1 on the far left and example field 4 on the far right. The modeled fields are shown for an altitude of 30 km and the sources were created with a magnetization of 0.45 A/m. The outline of the sources used to model the example fields is drawn in black.

The results from testing the example fields are shown in the tables below. For each of the source examples, the vector observed and calculated fields along with the along track difference observed and calculated fields were used. Each table includes the different depths at which equivalent dipoles were placed, the best-fitting inclination and declination at these depths, and the minimum RMS for each magnetic component. The correlation coefficient R of the best-fitting magnetization direction is provided and the maximum R value with its corresponding magnetization direction is also reported. The depth with the minimum radial RMS value is highlighted in yellow. If the overall maximum correlation coefficient is at a different depth, then its value and magnetization direction are highlighted in green. The minimum RMS and correlation coefficient results are consistent with each other most times, but sometimes there is a small difference between the results of two measures of similarity between the observed and modeled data sets as the phase information does not reflect the amplitudes and vice versa.

A. 2 Results of the tests

TABLE A.2: The results of testing the magnetization direction recovery methods on example field 1. For each depth of equivalent source dipoles, the best-fitting magnetization inclination and declination are shown with the RMS values for each component. The R value for the best-fitting direction based on minimum RMS and the maximum R value is given along with the magnetization direction associated with the maximum R value. The values based on minimum radial RMS are highlighted in yellow and if the overall maximum R value is at a different depth then this value is highlighted in green.

'Observed' Br

Depth	Inclination	Declination	Br_RMS	Bt_RMS	Bp_RMS	R Val	Max R	Max R Incl	Max R Decl
0	85	-35	0.605	0.45	0.404	0.9831	0.9831	85	-40
0	87	-45	0.605	0.449	0.403	0.9831	0.9831	87	-50
5	85	-65	0.639	0.462	0.43	0.9822	0.9822	85	-55
5	87	-35	0.636	0.461	0.426	0.9823	0.9823	87	-35
10	85	-175	1.139	0.666	0.861	0.9685	0.9685	85	-165
10	78	-8	1.135	0.662	0.861	0.9669	0.9675	90	-35

'Observed' ΔBr

Depth	Inclination	Declination	ΔBr_RMS	Δbt_RMS	ΔBp_RMS	R Val	Max R	Max R Incl	Max R Decl
0	85	-45	0.418	0.313	0.281	0.7068	0.7068	85	-45
0	85	-43	0.418	0.313	0.281	0.7068	0.7068	85	-43
5	85	60	0.418	0.314	0.281	0.7061	0.7061	85	60
5	87	32	0.418	0.314	0.281	0.7061	0.7061	87	32
10	85	85	0.42	0.315	0.282	0.7025	0.7025	85	65
10	87	73	0.42	0.315	0.282	0.7025	0.7025	87	58

Calculated Br

Depth	Inclination	Declination	Br_RMS	Bt_RMS	Bp_RMS	R Val	Max R	Max R Incl	Max R Decl
0	80	30	0.445	0.102	0.422	0.9927	0.9929	80	-180
0	82	26	0.443	0.093	0.425	0.9926	0.9928	79	3
5	85	40	0.474	0.162	0.397	0.9935	0.9936	85	-160
5	87	25	0.471	0.158	0.396	0.9935	0.9936	90	10
10	85	155	0.964	0.513	0.663	0.9879	0.988	85	170
10	78	-1	0.956	0.494	0.674	0.9864	0.9874	90	-30

Calculated ΔBr

Depth	Inclination	Declination	ΔBr_RMS	Δbt_RMS	ΔBp_RMS	R Val	Max R	Max R Incl	Max R Decl
0	85	50	0.009	0.007	0.005	0.9998	0.9998	85	50
0	85	51	0.009	0.007	0.005	0.9998	0.9998	85	51
5	85	50	0.017	0.013	0.009	0.9993	0.9993	85	50
5	87	31	0.017	0.013	0.009	0.9993	0.9993	87	30
10	85	25	0.046	0.034	0.024	0.9953	0.9953	85	25
10	85	27	0.046	0.034	0.024	0.9953	0.9953	84	26

TABLE A.3: The results of testing the magnetization direction recovery methods on example field 2. For each depth of equivalent source dipoles, the best-fitting magnetization inclination and declination are shown with the RMS values for each component. The R value for the best-fitting direction based on minimum RMS and the maximum R value is given along with the magnetization direction associated with the maximum R value. The values based on minimum radial RMS are highlighted in yellow and if the overall maximum R value is at a different depth then this value is highlighted in green.

'Observed' Br

Depth	Inclination	Declination	Br_RMS	Bt_RMS	Bp_RMS	R Val	Max R	Max R Incl	Max R Decl
0	75	55	0.201	0.147	0.137	0.9837	0.9837	75	55
0	73	51	0.201	0.147	0.137	0.9837	0.9837	74	54
5	70	40	0.201	0.148	0.137	0.9837	0.9837	75	40
5	72	47	0.201	0.147	0.137	0.9837	0.9837	72	49
10	70	45	0.202	0.148	0.137	0.9837	0.9837	70	40
10	71	43	0.202	0.148	0.137	0.9837	0.9837	72	40
15	75	35	0.243	0.163	0.171	0.9812	0.9812	75	35

'Observed' ΔBr

Depth	Inclination	Declination	ΔBr_RMS	Δbt_RMS	ΔBp_RMS	R Val	Max R	Max R Incl	Max R Decl
0	85	-45	0.142	0.104	0.096	0.6488	0.6488	90	-180
0	87	-48	0.142	0.104	0.096	0.6488	0.6488	87	-48
5	75	40	0.142	0.104	0.096	0.6481	0.6481	75	40
5	76	39	0.142	0.104	0.096	0.6481	0.6481	72	31
10	75	40	0.142	0.104	0.096	0.6476	0.6476	75	50
10	72	55	0.142	0.104	0.096	0.6476	0.6476	72	55
15	75	35	0.142	0.104	0.096	0.6468	0.6468	75	35
15	74	40	0.142	0.104	0.096	0.6468	0.6468	73	37
20	70	10	0.143	0.105	0.096	0.6423	0.6424	65	10
20	67	12	0.143	0.105	0.096	0.6424	0.6424	67	12

Calculated Br

Depth	Inclination	Declination	Br_RMS	Bt_RMS	Bp_RMS	R Val	Max R	Max R Incl	Max R Decl
0	60	50	0.159	0.09	0.135	0.9914	0.9919	70	80
0	59	52	0.159	0.09	0.136	0.9914	0.9919	67	80
5	55	50	0.16	0.1	0.129	0.9917	0.9923	70	75
5	56	50	0.16	0.099	0.129	0.9918	0.9923	69	75
10	65	55	0.167	0.097	0.132	0.9927	0.9928	65	60
10	65	53	0.166	0.098	0.131	0.9927	0.9928	65	59

Calculated ΔBr

Depth	Inclination	Declination	ΔBr_RMS	Δbt_RMS	ΔBp_RMS	R Val	Max R	Max R Incl	Max R Decl
0	75	55	0.005	0.003	0.003	0.9993	0.9994	70	60
0	74	55	0.005	0.003	0.003	0.9994	0.9994	73	55
5	75	65	0.006	0.005	0.004	0.9989	0.9989	70	55
5	73	66	0.006	0.005	0.004	0.9989	0.9989	70	55
10	70	65	0.008	0.006	0.005	0.9982	0.9982	70	60
10	71	62	0.008	0.006	0.005	0.9982	0.9982	70	62

TABLE A.4: The results of testing the magnetization direction recovery methods on example field 3. For each depth of equivalent source dipoles, the best-fitting magnetization inclination and declination are shown with the RMS values for each component. The R value for the best-fitting direction based on minimum RMS and the maximum R value is given along with the magnetization direction associated with the maximum R value. The values based on minimum radial RMS are highlighted in yellow and if the overall maximum R value is at a different depth then this value is highlighted in green.

'Observed' Br

Depth	Inclination	Declination	Br_RMS	Bt_RMS	Bp_RMS	R Val	Max R	Max R Incl	Max R Decl
0	80	140	0.12	0.084	0.082	0.982	0.982	80	145
0	81	143	0.12	0.084	0.082	0.982	0.982	81	143
5	80	135	0.118	0.084	0.081	0.982	0.982	80	145
5	82	141	0.118	0.084	0.081	0.982	0.982	82	140
10	80	150	0.117	0.084	0.081	0.982	0.982	80	150
10	82	142	0.117	0.084	0.081	0.982	0.982	82	143
15	85	135	0.117	0.084	0.081	0.9819	0.9819	85	135
15	83	141	0.117	0.084	0.081	0.9819	0.9819	83	141
20	85	135	0.117	0.084	0.081	0.9819	0.9819	85	140
20	83	132	0.117	0.084	0.081	0.9819	0.9819	83	133
25	85	145	0.118	0.084	0.081	0.9819	0.9818	85	140
25	83	134	0.118	0.084	0.081	0.9819	0.9819	83	137

'Observed' ΔBr

Depth	Inclination	Declination	ΔBr_RMS	Δbt_RMS	ΔBp_RMS	R Val	Max R	Max R Incl	Max R Decl
0	80	155	0.083	0.058	0.057	0.5414	0.5414	80	155
0	81	154	0.083	0.058	0.057	0.5415	0.5414	81	154
5	75	110	0.083	0.058	0.057	0.5403	0.5403	75	115
10	55	95	0.083	0.059	0.057	0.5397	0.5397	55	95
15	70	95	0.083	0.059	0.057	0.5394	0.5394	70	95
20	85	150	0.083	0.059	0.057	0.5394	0.5394	80	150
20	84	153	0.083	0.059	0.057	0.5394	0.5394	82	147
25	80	125	0.083	0.059	0.057	0.5392	0.5392	80	125
25	82	134	0.083	0.059	0.057	0.5392	0.5392	82	134
30	85	110	0.083	0.059	0.057	0.5388	0.5388	85	110
30	85	113	0.083	0.059	0.057	0.5388	0.5388	85	111
35	85	70	0.083	0.059	0.057	0.5359	0.5359	85	45
35	86	64	0.083	0.059	0.057	0.5359	0.5359	84	50
40	80	10	0.083	0.059	0.057	0.5307	0.5308	75	30
40	77	3	0.083	0.059	0.057	0.5309	0.5309	77	2
45	75	-20	0.084	0.06	0.057	0.5237	0.5237	75	-20

Calculated Br

Depth	Inclination	Declination	ΔBr_RMS	Δbt_RMS	ΔBp_RMS	R Val	Max R	Max R Incl	Max R Decl
0	55	150	0.167	0.053	0.155	0.9652	0.9652	55	150
5	55	145	0.16	0.046	0.151	0.9666	0.9667	60	150
10	55	135	0.155	0.042	0.147	0.9682	0.9682	60	145
15	55	130	0.151	0.038	0.143	0.9699	0.9701	55	110
15	57	130	0.15	0.037	0.143	0.9701	0.9703	58	112
20	60	110	0.145	0.041	0.136	0.973	0.973	60	110
20	59	107	0.144	0.042	0.135	0.9731	0.9732	59	112
25	65	100	0.145	0.045	0.132	0.9734	0.9731	65	110
25	66	98	0.145	0.045	0.132	0.9734	0.9735	67	108
30	65	125	0.185	0.059	0.147	0.9723	0.9723	65	125
30	67	126	0.184	0.058	0.148	0.972	0.9723	64	125

Calculated ΔBr

Depth	Inclination	Declination	ΔBr_RMS	Δbt_RMS	ΔBp_RMS	R Val	Max R	Max R Incl	Max R Decl
0	80	115	0.001	0.001	0.001	0.9997	0.9997	80	115
0	80	115	0.001	0.001	0.001	0.9997	0.9997	80	115
5	85	-180	0.002	0.002	0.001	0.9994	0.9994	85	-180
5	85	-180	0.002	0.002	0.001	0.9994	0.9994	85	-180
10	85	-170	0.003	0.002	0.002	0.999	0.999	85	-170
10	83	-144	0.003	0.002	0.002	0.999	0.999	83	-143

TABLE A.5: The results of testing the magnetization direction recovery methods on example field 4. For each depth of equivalent source dipoles, the best-fitting magnetization inclination and declination are shown with the RMS values for each component. The R value for the best-fitting direction based on minimum RMS and the maximum R value is given along with the magnetization direction associated with the maximum R value. The values based on minimum radial RMS are highlighted in yellow and if the overall maximum R value is at a different depth then this value is highlighted in green.

'Observed' Br

Depth	Inclination	Declination	Br_RMS	Bt_RMS	Bp_RMS	R Val	Max R	Max R Incl	Max R Decl
0	-5	-25	0.289	0.234	0.169	0.9892	0.9892	-5	-25
0	-5	-25	0.289	0.234	0.169	0.9892	0.9892	-5	-25
5	-5	-25	0.3	0.239	0.174	0.9886	0.9886	-5	-25
5	-5	-24	0.299	0.238	0.173	0.9887	0.9887	-5	-24

Observed' ΔBr

Depth	Inclination	Declination	ΔBr_RMS	Δbt_RMS	ΔBp_RMS	R Val	Max R	Max R Incl	Max R Decl
0	-5	-25	0.203	0.166	0.118	0.7182	0.7182	-5	-25
0	-6	-26	0.203	1.166	0.118	0.7183	0.7183	-6	-23
5	-5	-25	0.203	0.166	0.118	0.7171	0.7171	-5	-25
5	-4	-23	0.203	0.166	0.118	0.7172	0.7172	-4	-23
10	-5	-25	0.204	0.167	0.118	0.716	0.716	-5	-25
10	-6	-23	0.204	0.167	0.118	0.7161	0.7161	-6	-23

Calculated Br

Depth	Inclination	Declination	Br_RMS	Bt_RMS	Bp_RMS	R Val	Max R	Max R Incl	Max R Decl
0	-5	-25	0.119	0.026	0.11	0.9982	0.9982	-5	-25
0	-6	-24	0.113	0.028	0.102	0.9984	0.9985	-6	-24
5	-5	-25	0.149	0.068	0.118	0.9975	0.9975	-5	-25
5	-6	-23	0.134	0.067	0.099	0.998	0.998	-7	-23

Calculated ΔBr

Depth	Inclination	Declination	ΔBr_RMS	Δbt_RMS	ΔBp_RMS	R Val	Max R	Max R Incl	Max R Decl
0	-5	-25	0.007	0.005	0.005	0.9995	0.9995	-5	-25
0	-6	-23	0.006	0.004	0.0014	0.9996	0.9996	-6	-23
5	-5	-25	0.011	0.009	0.006	0.9988	0.9988	-5	-25
5	-4	-23	0.01	0.008	0.006	0.9991	0.9991	-4	-23

The above tables show the best-fitting magnetization directions along with the minimum radial RMS value and correlation coefficient. The best-fitting direction based on minimum RMS did not always give the maximum correlation coefficient so the magnetization direction recovered from the maximum correlation coefficient is also included. The best fitting-depth was found by increasing the depth until the radial RMS value was a minimum. If there were multiple depths with the same RMS value, then the deepest depth was used for simplicity but in the future it needs to be tested if averaging all results with the same minimum RMS would give a better best-fitting magnetization direction. When using actual vector and gradient fields the RMS values were always different for different depths. From the results, it is seen that minimizing observed Br and ΔBr RMS both give good results but that minimizing observed ΔBr RMS recovers the depth of the source better. Even though the correlation coefficients are overall much lower for the comparisons with ΔBr RMS than Br RMS, with actual vector fields the noise can be significant and bias the results. Along-track differences of the vector fields are much less noisy with real data and therefore when the vector fields are contaminated by external fields, minimum ΔBr RMS would be useful.

Using the calculated field and minimizing ΔBr RMS also gives good results. The above results show that minimizing Br RMS can give a much lower best-fitting inclination value if the source has a high inclination. Since this field did not consistently produce good results, it was not used when finding the magnetization direction of lunar swirl magnetic anomalies. Based on the above comparisons, it was

decided to use the observed and calculated gradient fields for comparison with the modeled equivalent source dipole gradient fields.

It is also interesting to note that the minimum radial RMS value seems to recover the inclination value well but does not consistently recover the declination at high inclination values. This is because there is more ambiguity in the declination when the inclination is near vertical and many declination values will produce similar fields. Only looking at the radial component does not constrain the declination value well, but minimizing the theta RMS could provide a better estimate of the declination value when the inclination is high. The declination values used in the example fields are mainly north-south. If the declination was more east-west, then the B_ϕ would also be needed. From the above tables it can be seen that when the inclination is near vertical, the depth with the minimum theta RMS value usually gives a better estimate on the declination. A best estimate for the declination value could be recovered by minimizing the theta and phi components and then using the best-fitting depth and holding the declination value constant to recover an inclination value. Future testing needs to be done to check that this result would give reliable results.

Along with the minimum RMS value, the maximum R was also considered. In most cases, the minimum RMS and maximum R for the best-fitting depth are very similar. The overall maximum R for multiple depths was also examined. For each example field and method used, the magnetization direction found from the overall maximum R and the magnetization from the maximum R at the best-fitting depth were compared. The results are shown in the above tables and are highlighted in green. When the overall maximum and the maximum from the best-fitting depth were the same the result was highlighted in yellow. These results show that while the two recovered magnetization directions are often the same, that using the maximum correlation coefficient from the best-fitting depth gives a more accurate result more frequently than using the overall maximum value. As a result, only the maximum R value from the best-fitting depth was used to find the best-fitting magnetization direction. The p-values (level of significance) associated with the correlation coefficients were always <0.01.

The testing process could be improved by finding a better method to add noise to the data. Currently, Gaussian noise is added to the data but it is random noise and does not mimic the noise seen in the LP observed data well. As a result of using random noise, the along track difference fields actually contain more noise in comparison with the vector fields. This could be the reason that when testing, the observed vector data gives better results than the observed along track difference data. Even with the issues with the added noise, the testing process shows that the method of using the observed and calculated gradient fields are able to recover a magnetization direction that is close to the simulated value and is able to estimate the depth of the source when using the observed gradient field. This model study confirms that the methods 1 and 2 described in section 2 of this paper produces good results and the reasoning presented here also explains why the calculated vector data was not used in the determination of magnetization directions in the study.

B.1 Paleopole location calculations

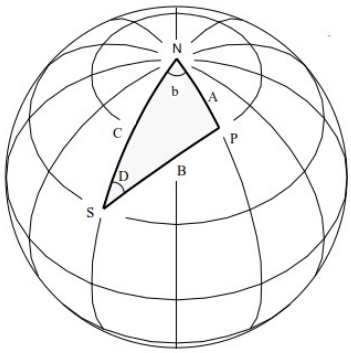

FIG. B.1: The spherical triangle used to calculate the paleopole location. Figure edited from Butler, 1992.

The paleopole location was calculated using a spherical triangle, illustrated in Figure B.1. A is the angular distance from geographic North pole to the paleopole location, B is the angular distance from the site location to paleopole location, and C from the site location to geographic North pole. In the equations below, I represents the anomaly's magnetization inclination, D the magnetization declination, lat_S and lon_S are the anomaly site locations, and lat_P and lon_P give the coordinates of the paleopole. The angle measurements are in degrees. When the calculated B is negative, 180° is added to the value to make it positive for the determination of the north paleopole (in Butler's textbook, a negative inclination leads to the south paleopole). The half angle formula for spherical triangles was used to calculate b.

$$B = \arctan\left(\frac{2}{\tan(I)}\right)$$

$$lat_P = \arcsin\left(\sin(lat_S)\cos(B) + \cos(lat_S)\sin(B)\cos(D)\right)$$

$$A = 90 - lat_P; \qquad C = 90 - lat_S; \qquad S = \frac{(A+B+C)}{2};$$

$$b = 2\arcsin\left(\frac{\sqrt{(\sin(S-A)\sin(S-C))}}{\sin(A)\sin(C)}\right)$$

If the value of the declination was negative then the paleopole longitude was found by subtracting b from the site's longitude.

$$lon_P = lon_S - b$$

If the value of the declination was positive, then b was added to the site's longitude.

$$lon_P = lon_S + b$$